# The Impact of Plate Motions on Long-Wavelength InSAR-Derived Velocity Fields

**Oliver L. Stephenson[1], Yuan-Kai Liu[1], Zhang Yunjun[1], Mark Simons[1], and Paul Rosen[2]**

[1]Seismological Laboratory, Division of Geological and Planetary Sciences, California Institute of

Technology, Pasadena, CA 91125, USA.

[2]Jet Propulsion Laboratory, California Institute of Technology, Pasadena, CA 91109, USA.

**Key Points:**

- Interferometric synthetic aperture radar (InSAR) time series are sensitive to uniform horizontal and vertical plate motions
- Such motions create long-wavelength spatial gradients that are visible in InSAR-derived velocity maps after removing other signals
- Plate motion effects can be easily accounted for using plate motion models, allowing long-wavelength deformation to be more clearly seen

Corresponding author: Oliver L. Stephenson, `olstephe@caltech.edu`

**Abstract**

Interferometric Synthetic Aperture Radar (InSAR) measurements are increasingly being used to measure small amplitude tectonic deformations over large spatial scales. Residual signals are often present at these scales, and are interpreted to be noise of indeterminate origin, limiting studies of long-wavelength deformation. Here, we demonstrate the impact of bulk motion by the Earth's tectonic plates on InSAR-derived velocity fields. The range-dependent incidence angle of the InSAR observations, coupled with plate velocities of centimeters per year, can induce long-wavelength spatial gradients of millimeters per year over hundreds of kilometers in InSAR-derived velocity fields. We show that, after applying corrections, including for the ionosphere and troposphere, plate motion represents the dominant source of long-wavelength secular velocity gradients in multi-year time series for several study areas. This signal can be accounted for using plate motion models, allowing improved detection of regional tectonic strain at continental scales.

**Plain Language Summary**

Interferometric Synthetic Aperture Radar (InSAR) relies on repeat radar imaging to measure small motions of the Earth's surface. These motions can be used to understand a range of processes happening below the surface, from hydrology to tectonics. We show how the slow motion of Earth's tectonic plates can create a signal in InSAR data that may be confused with local tectonic signals. We also demonstrate a simple method for removing this signal, making InSAR more useful for studying very small motions over large areas of the Earth, especially in regions where we do not have good observations from other sources.

# 1 Introduction

Interferometric Synthetic Aperture Radar (InSAR) is an active imaging technique for measuring ground displacements that occur between repeat passes of an imaging platform, such as a satellite (e.g. Massonnet and Feigl (1998); Hanssen (2001); Simons and Rosen (2015)). InSAR deformation measurements are generally expressed relative to a single point, or ensemble of points, within the imaged area, usually assumed to be stable through time (e.g. Mahapatra et al. (2018)). While InSAR has been used extensively

for measuring large amplitude ($> 1$ cm), deformation over short-wavelengths ($< 100$ km) (e.g. Massonnet et al. (1993); Merryman Boncori (2019)), other signals present in the data challenge our ability to measure deformation at the scale of millimeters per year over hundreds of kilometers.

InSAR observations at long wavelengths are the combination of motion of the Earth's surface, changes in the atmosphere, and measurement and processing errors. The Earth motion signals comprise the surface deformation of interest, e.g. from tectonic strain, volcanic activity or subsidence (Massonnet et al. (1993); Massonnet and Feigl (1998); Amelung et al. (1999)), along with solid Earth tides (SET) (X. Xu & Sandwell, 2020), and ocean tidal loading (Dicaprio et al., 2008). Atmospheric signals come from propagation delay through the ionosphere (Z.-W. Xu et al., 2004) and troposphere (Tarayre & Massonnet, 1996). Errors sources include the satellite orbits (Massonnet & Feigl, 1998), local oscillator drift (Marinkovic & Larsen, 2015), phase unwrapping (Biggs et al., 2007) and topography (Berardino et al., 2002).

These effects can obscure small amplitude, long-wavelength signals in InSAR due to local tectonic processes, such as surface deformation from interseismic loading (e.g. Fournier et al. (2011); Parizzi et al. (2021)). Thus, it is common to not interpret long-wavelength signals from InSAR alone, instead removing them by empirically fitting 2D polynomial functions, known as "ramps", to the data (e.g. Fialko (2006); Jolivet et al. (2015)), or combining InSAR velocities with Global Navigation Satellite System (GNSS) measurements in order to constrain the long-wavelength deformation (e.g. Weiss et al. (2020); X. Xu et al. (2021); Neely et al. (2020); Parizzi et al. (2020)). Such approaches are limiting when we wish to measure large-scale deformation in regions of sparse GNSS coverage (Chaussard et al., 2016; Neely et al., 2020).

The quality of InSAR data and correction methods have substantially increased over the last several years. The European Space Agency's (ESA) Sentinel-1 satellites have been regularly acquiring data for significant portions of the planet since late 2014. Sentinel-1 offers the advantages of improved orbital controls and uncertainties, reducing the noise contribution from satellite orbits (Fattahi & Amelung, 2014), as well as unrestricted data access. Split-band processing now allows for the estimation of the ionospheric signal directly from the InSAR data (Gomba et al., 2016; Fattahi, Simons, & Agram, 2017; Liang et al., 2019), and higher quality weather models have improved the correction of tropo-

spheric phase (Li et al., 2005; Doin et al., 2009; Jolivet et al., 2011). Techniques for removing the SET (X. Xu & Sandwell, 2020) and ocean tidal loading signals (Dicaprio et al., 2008; Yu et al., 2020) have also been developed, among other correction methods. After corrections, there may still be long-wavelength residuals in multi-year Sentinel-1 time series, including from the troposphere, which can contribute up to 5 mm/yr over 150 km (Parizzi et al., 2021), and orbital errors, contributing around 0.5 mm/yr over 100 km for Sentinel-1 (Fattahi & Amelung, 2014).

In this work, we focus on the contribution of coherent uniform motion of Earth's tectonic plates to the long-wavelength component of InSAR-derived velocity fields. The satellite line-of-sight (LOS) vector varies systematically in the satellite range direction (i.e. across the satellite track). causing a changing sensitivity to ground deformation with range. Bulk motion of tectonic plates in the satellite frame of reference, coupled with this LOS variation, can create quasi-linear gradients in InSAR-derived velocity fields, resulting in ramps, predominantly in the satellite range direction. This effect has been noted before, e.g., by Bähr et al. (2012), Bähr (2013) and Parizzi et al. (2020). Here, we demonstrate that plate motion creates ramps of several millimeters per year, across the 250 km track width, in six multi-year Sentinel-1 InSAR time series. After other corrections have been applied, plate motion is the dominant long-wavelength signal in our data, and we show that this signal can be straightforwardly compensated for using plate motion models. This adjustment is not currently part of several open-source InSAR time series analysis packages (e.g Hooper et al. (2012); Agram et al. (2013); Yunjun et al. (2019); Morishita et al. (2020)), and we provide an implementation of the method in the MintPy package (Yunjun et al., 2019).

## 2 The Reference Frame of InSAR Measurements

Quantifying ground deformation using InSAR requires a precise measurement of the satellite orbit ephemerides (Fattahi & Amelung, 2014; Peter, 2021). For Sentinel-1 the orbit is measured with respect to the International Terrestrial Reference Frame (ITRF) (Peter, 2021), an Earth-centered, Earth-fixed reference frame in which there is no net rotation of the Earth's surface (Altamimi et al., 2016). Observations of absolute ground motion relative to the satellite are therefore also in ITRF (Bähr et al., 2012; Lazecky & Hooper, 2022).

108 However, it is not possible for InSAR to record absolute motions due to the $2\pi$ am-
109 biguity in the interferometric phase (e.g. Massonnet and Feigl (1998)). Instead, displace-
110 ment measurements are generally expressed relative to a reference point within the im-
111 aged region, assumed to be stationary. Velocities can then be obtained from functional
112 fits to displacement time series, with inferred velocities also expressed relative to this point.

Selecting the reference point is not equivalent to expressing the InSAR velocities
in a reference frame moving with that point (Bähr et al., 2012; Bähr, 2013). We must
therefore consider how velocities in ITRF appear in the InSAR deformation field. We
represent the 3D ITRF secular velocity field of the Earth's surface as:

$$\boldsymbol{v}(\boldsymbol{x}) = \boldsymbol{v}_p(\boldsymbol{x}) + \boldsymbol{v}_d(\boldsymbol{x}). \tag{1}$$

113 $\boldsymbol{v}_p(\boldsymbol{x})$ is the velocity field due to the strain-free motion of the relevant rigid plate in ITRF,
114 and $\boldsymbol{v}_d(\boldsymbol{x})$ is the velocity due to internal deformation of the plate, for example due to
115 tectonic, volcanic, or hydrological processes.

Defining the LOS unit vector pointing from the ground to the satellite as $\hat{\boldsymbol{l}}(\boldsymbol{x})$, the
LOS projection of the 3D velocity field, minus the InSAR reference velocity, can be writ-
ten as:

$$\boldsymbol{v}_l(\boldsymbol{x}) = \boldsymbol{v}(\boldsymbol{x}) \cdot \hat{\boldsymbol{l}}(\boldsymbol{x}) - \boldsymbol{v}(\boldsymbol{x}') \cdot \hat{\boldsymbol{l}}(\boldsymbol{x}'), \tag{2}$$

116 where the reference is at point $\boldsymbol{x}'$. $\boldsymbol{v}_l(\boldsymbol{x})$ is the secular velocity that will be measured by
117 the satellite, assuming all other signals and noise can be neglected.

In ITRF, $\boldsymbol{v}_l(\boldsymbol{x})$ has a contribution from the plate motion, which we can write as:

$$\boldsymbol{v}_{l,p}(\boldsymbol{x}) = \boldsymbol{v}_p(\boldsymbol{x}) \cdot \hat{\boldsymbol{l}}(\boldsymbol{x}) - \boldsymbol{v}_p(\boldsymbol{x}') \cdot \hat{\boldsymbol{l}}(\boldsymbol{x}'). \tag{3}$$

118 The second term, from the reference, is constant, while the first term depends on the spa-
119 tial variation of $\boldsymbol{v}_p(\boldsymbol{x})$ and $\hat{\boldsymbol{l}}(\boldsymbol{x})$. The LOS vector $\hat{\boldsymbol{l}}(\boldsymbol{x})$ can vary substantially over an im-
120 age swath. For Sentinel-1, the incidence angle (the angle between the LOS and the ver-
121 tical) varies approximately from 29° in the near range to 46° in the far range over the
122 250-km-width of the imaging swath (for data acquired in Interferometric Wideswath mode).
123 The range-dependent variation in $\hat{\boldsymbol{l}}(\boldsymbol{x})$ implies a changing sensitivity to components of
124 the 3D deformation field across the track, with sensitivity to horizontal motion increas-
125 ing and vertical motion decreasing as we move from near range to far range. This range-
126 dependent sensitivity causes uniform plate motions to appear as velocity ramps in the
127 range direction when projected into the satellite LOS (Figure 1).
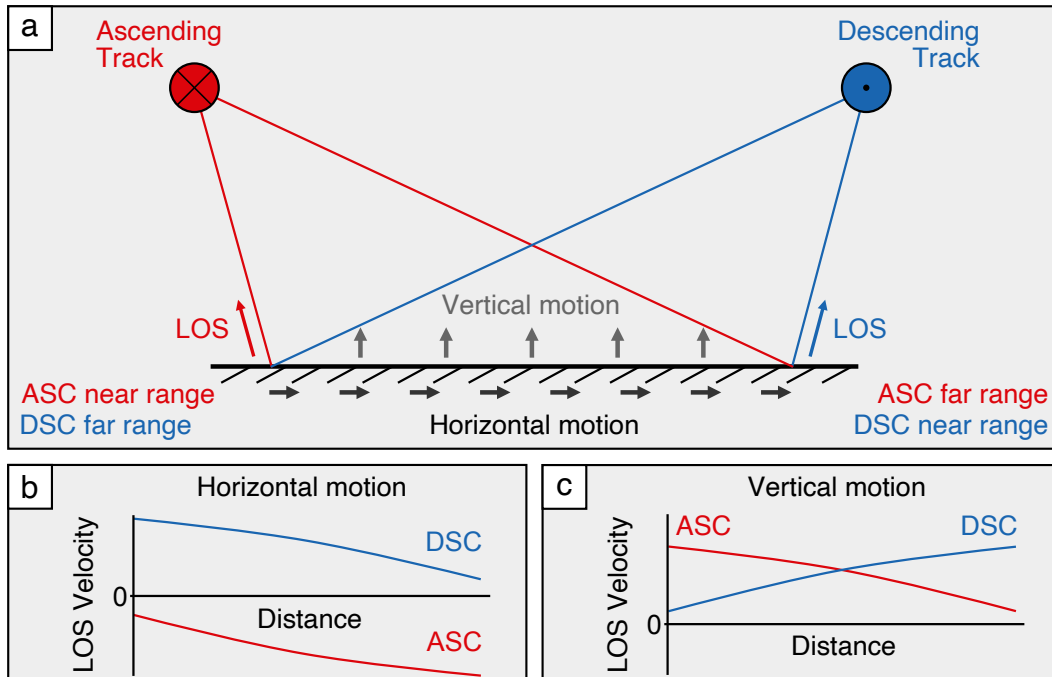
**Figure 1.** Illustration of how uniform horizontal and vertical motions result in ramps in InSAR-derived velocity measurements. **(a)** Satellite images acquired from ascending (ASC) and descending (DSC) orbital tracks, which have a varying LOS incidence angle across the track. The term "range" refers to the distance from the ground target to the satellite, with near range and far range the closest and furthest points from the satellite respectively. Red and blue arrows represent the ground-to-satellite LOS vector in the near range for ASC and DSC tracks, respectively. Grey and black arrows represent plate motion in the reference frame of the satellite. For illustration purposes we assume the ASC and DSC tracks are parallel to each other but in opposite directions, ignore Earth curvature. Figure not to scale. **(b)** Profile of the horizontal plate velocity projected into the LOS of the ASC and DSC tracks, against geographic distance along the ground. **(c)** Same as (b), except for vertical plate motion, resulting in opposite gradients in the LOS profiles. The observing geometry creates a small curvature in all profiles, which is exaggerated in the figure. For InSAR measurements, the LOS velocity is expressed relative to a point within the image, so each of these profiles would be vertically shifted to intersect with the $x$ axis at the chosen reference point.

128      The plate velocity, $\boldsymbol{v}_p(\boldsymbol{x})$, also varies over an image swath. The motion of a rigid

129 plate on Earth's surface can be represented by a rotation rate about an axis, known as

130 an Euler pole (McKenzie & Parker, 1967). Given the angular velocity of a chosen plate,

131 $\boldsymbol{\Omega}$, we can write the velocity of any point, $\boldsymbol{x}$, on that plate as $\boldsymbol{v}_p(\boldsymbol{x}) = \boldsymbol{\Omega} \times \boldsymbol{x}$, where

132 $\times$ is the cross product. Thus, the velocity field due to rigid plate motion varies with dis-

133 tance from the plate's Euler pole. This variation in $\boldsymbol{v}_p(\boldsymbol{x})$ also contributes to the long-

134 wavelength LOS velocity field.

135      Because of the effect of plate motions, InSAR velocity measurements should not

136 generally be considered to be in a local reference frame, despite the use of a local ref-

137 erence point. Choosing a reference point within an InSAR image offsets InSAR veloc-

138 ity measurements from the LOS projection of ITRF velocities by an unknown constant

139 (Equation 1), but does not remove the long-wavelength gradients that can be induced

140 by plate motion (Equation 3). If ITRF plate motion is negligible when projected to the

141 LOS, and does not vary substantially over the InSAR track, or the satellite LOS vari-

142 ation across the track is small, then $\boldsymbol{v}_{l,p}(\boldsymbol{x}) \approx 0$. Choosing a reference point that is sta-

143 ble with respect to the plate is then approximately equivalent to putting the InSAR ve-

144 locities into the reference frame of that plate, however this should not be generally as-

145 sumed.

146      Several authors have investigated the reference frame of InSAR observations, gen-

147 erally in the context of using GNSS to put InSAR measurements into a terrestrial ref-

148 erence frame (e.g. Mahapatra et al. (2018); Johnston et al. (2021)). The influence of plate

149 motion on InSAR velocities has been noted by Bähr et al. (2012) and Bähr (2013), who

150 term it the *reference frame effect*. Bähr et al. (2012) present this phenomenon in terms

151 of a temporally increasing correction to the interferometric baseline, while Bähr (2013)

152 notes that this can also be framed in terms of the varying satellite LOS causing differ-

153 ing sensitivity to plate motion (the approach taken here). Parizzi et al. (2020) used plate

154 motion models to adjust their LOS velocity fields after merging InSAR with GNSS. Au-

155 thors have also noted the impact of plate motions on SAR geolocation accuracy (Cong

156 et al. (2012)). Our focus here is to demonstrate that plate motions can explain a signif-

157 icant fraction of observed residual long-wavelength surface velocities, after other correc-

158 tions have been applied, and without combining InSAR data with GNSS.

## 3 Data and Methods

### 3.1 Data Processing

We present several examples using InSAR data from the ESA's Sentinel-1 satellites, taken from ascending (ASC) and descending (DSC) tracks covering the Makran subduction zone (Iran), the Gulf of Aqaba (at the northern end of the Red Sea), and western Australia. For each track, we process at least 5 years of data using the InSAR Scientific Computing Environment (ISCE) (Rosen et al., 2012; Fattahi, Agram, & Simons, 2017). After forming the interferogram networks, we create deformation time series using MintPy (Yunjun et al., 2019).

Before examining residual signals due to plate motion, we apply corrections for the ionosphere, troposphere, SET, and digital elevation model (DEM) error. We use split-band processing to correct for the ionosphere (Liang et al., 2019), PyAPS and the ERA5 weather model to mitigate the tropospheric delay (Jolivet et al., 2014; Hersbach et al., 2020), the method of Fattahi and Amelung (2013) for DEM error correction and PySolid to correct for SET (Milbert, 2018; Yunjun et al., 2022). Further details of our data and processing are presented in the supporting information (Text S1, S2 and Table S1).

### 3.2 Adjusting InSAR Measurements for Plate Motion

After all other corrections have been applied, we can then observe and account for the signal of plate motion. InSAR observations of ground motion are generally used to study regional deformation, rather than plate translations or rotations. For such purposes, a useful reference frame is one that moves with the plate in which we are trying to measure strain. Translating into this reference frame requires us to remove the signal of plate motion in the satellite's frame of reference, i.e. ITRF (Bähr, 2013; Parizzi et al., 2020).

GNSS networks can be used to connect InSAR measurements to ITRF (e.g. Mahapatra et al. (2018); Johnston et al. (2021)), which can then be transformed into a reference frame moving with the chosen plate. In the absence of sufficient GNSS coverage, we can estimate the transformation into the plate's frame of reference using the following steps:

1. Choose an InSAR reference point, $\boldsymbol{x}'$, that is stable with respect to the plate
2. Find the velocity field of the plate within ITRF, i.e. $\boldsymbol{v}_p(\boldsymbol{x})$

3. Project that velocity field into the satellite LOS direction

4. Subtract the LOS velocity of the reference point, $\boldsymbol{v}_{l,p}(\boldsymbol{x'})$, from the projected plate velocity to compute $\boldsymbol{v}_{l,p}(\boldsymbol{x})$, which is then removed from the InSAR velocity map.

Note that, after these steps, InSAR-derived velocities are still expressed relative to a reference point, meaning that deformation and other signals seen at the reference point will still affect the entire scene.

We use the geodetically constrained ITRF plate motion model of Altamimi et al. (2017) to estimate the plate velocity field. For each study region, we identify our reference plate (Table S1), then use the modeled angular velocity of the plate to calculate horizontal velocities for our observation region. We then project these velocities into the LOS direction and remove them from the velocity map.

## 4 Results

### 4.1 The Importance of Removing Other Signals for Revealing Plate Motion

We expect plate motion to contribute below 8 mm/yr across the 250 km width of the Sentinel-1 tracks for our chosen regions (Figure S6), making it important to remove other signals to show what fraction of the residual velocity can be explained by plate motion. For ASC tracks in the Makran and Gulf of Aqaba, ionosphere corrections have a particularly large effect on the long-wavelength velocity signal (e.g. contributing a 25 mm/yr ramp along track 86 for the Makran, Figure 2), with DSC tracks showing substantially less ionospheric signal. ASC tracks are acquired at dusk—a period of greater ionosphere activity than dawn, when DSC tracks are acquired. This impact is still notable in C-band Sentinel-1 data, even though it suffers much less from ionospheric effects than L-band (Fattahi, Simons, & Agram, 2017; Liang et al., 2019).

We find that troposphere corrections have a less significant impact on the long-wavelength velocity signal than the ionosphere for ASC tracks, and a comparable effect for DSC tracks. Corrections for the SET have a small effect on the long-wavelength secular velocity, contributing below 0.5 mm/yr over several hundred kilometers. The range of DEM error corrections is less than $\pm 0.5$ mm/yr in our results and has a minimal contribution to the

long-wavelength velocity field. We show the impact of the above corrections for all tracks in Figures 2 and S1-S5, and present more details in Text S2.

### 4.2 The Impact of Accounting for Plate Motion

After applying the suite of corrections we are left with residual velocity ramps in all of our tracks, predominantly in the range direction. We present the results of plate motion adjustments for several tracks in Figures 3 and 4. Our results show that accounting for plate motion removes a significant fraction of the residual velocity ramp in every case, reducing the across-track ramps from 4-7 mm/yr/track to below 1.5 mm/yr/track. For our data the plate motion signal is comparable to the troposphere in its effect on the long-wavelength velocity field.

The proximity of the Arabian plate Euler pole to the Gulf of Aqaba study area results in the plate velocity field varying appreciably within the tracks (Altamimi et al., 2017). This variation causes an additional LOS velocity ramp along the track, with an opposite direction for the ascending and descending tracks. Figures 4 (a) and (b) show how this along track gradient can be clearly seen in the data, and is well corrected for by the plate motion model. We do not see similar along-track ramps for Australia and Makran, which is consistent with the plate motion velocity field.

## 5 Discussion

Other authors have previously noted that plate motion will affect InSAR velocity measurements (e.g. Bähr et al. (2012)), however the narrower variation of the satellite LOS angle for earlier satellites, more limited data, and the presence of other significant long-wavelength signals, has made the signal difficult to isolate. The quality of recently available data and correction methods, and the wide swath of Sentinel-1, allow us to show the plate motion signal and the clear impact of accounting for it. Our results from the Gulf of Aqaba illustrate that plate rotation is an important part of the correction.

After adjusting for plate motion, remaining long-wavelength signals could be due to the incomplete removal of some signals (predominantly the troposphere (Fattahi & Amelung, 2015; Parizzi et al., 2021)), sources that we have not corrected for (e.g. ocean tidal loading (Dicaprio et al., 2008) and orbital errors (Fattahi & Amelung, 2014)), or actual strain accumulation in the lithosphere—the signal that InSAR measurements of-
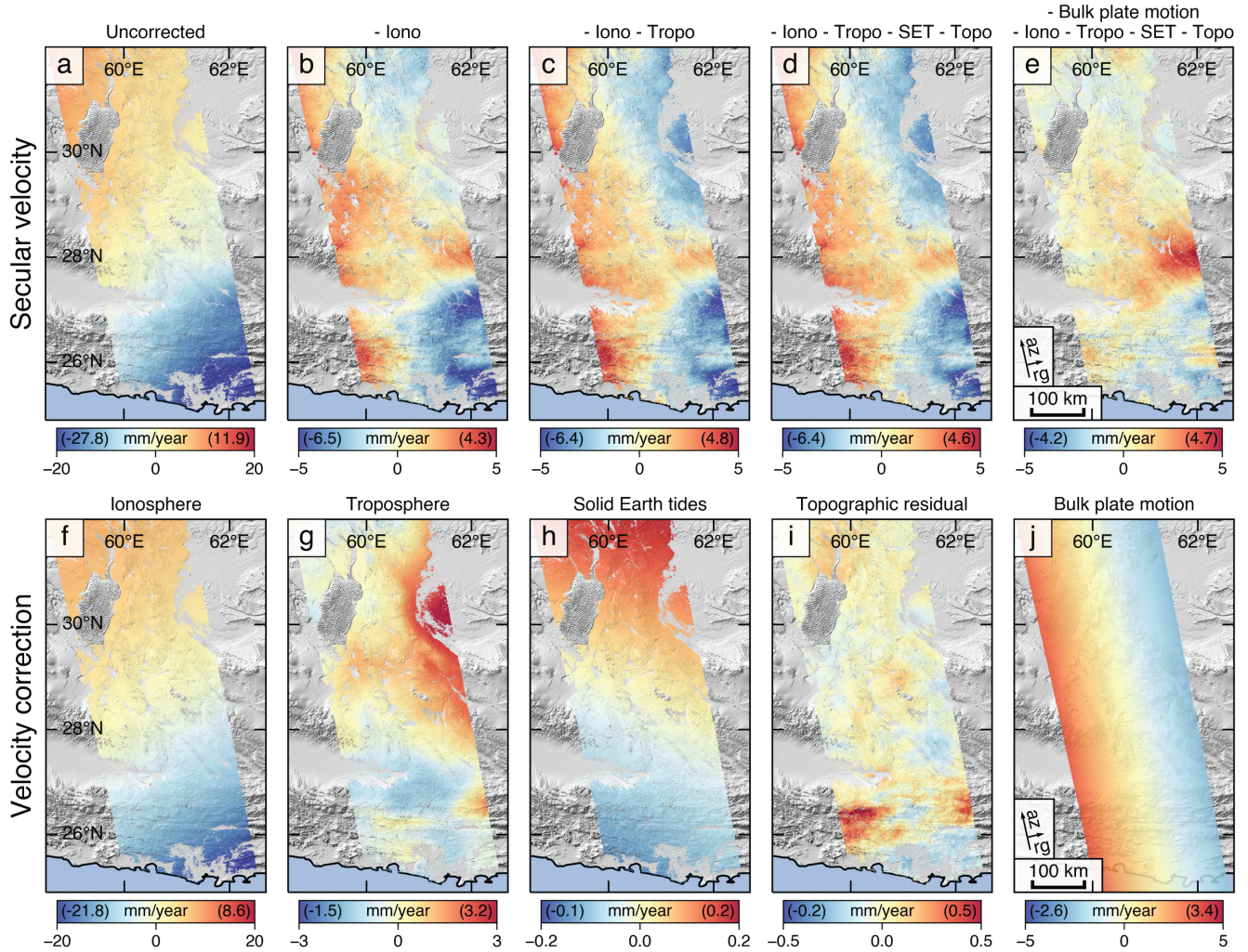
**Figure 2.** Cumulative impact of corrections on the InSAR-derived velocity field for Sentinel-1, track 86 (ASC) over the Makran subduction zone. For plotting purposes, we remove the median value from each velocity field. Positive values represent apparent motion towards the satellite. Color bars are re-scaled between plots. Numbers in parentheses within the color bars refer to the 2nd and 98th percentiles of the velocity. "az" is the azimuth direction (satellite direction of motion), and "rg" the range direction (perpendicular to the satellite direction of motion). **(a)** No corrections applied. **(b)** Estimated ionosphere removed. **(c)** Tropospheric model removed. **(d)** SET model removed and DEM error (Topo) correction applied. **(e)** Plate motion correction applied. The positive signal around (28 °N, 62 °E) is post-seismic deformation from the 2013 Khash earthquake (Barnhart et al., 2014). **(f)** Applied ionospheric correction. **(g)** Applied tropospheric correction. **(h)** Applied SET correction. **(i)** Applied DEM error correction. Larger signals in the south may be bias from tropospheric residuals (Fattahi & Amelung, 2014). **(j)** Applied plate motion correction.
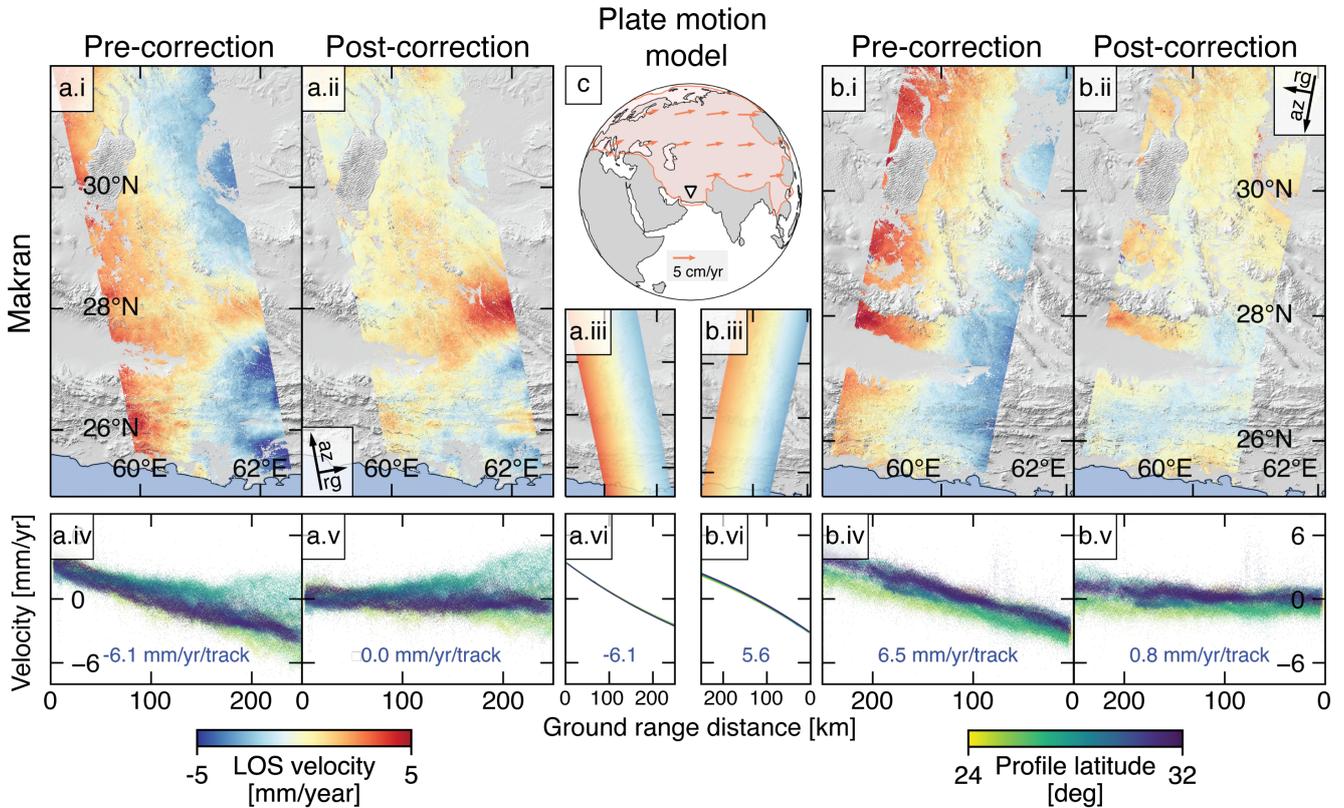
**Figure 3.** The impact of plate motion adjustments for InSAR tracks over the Makran subduction zone. For plotting purposes, we remove the median from each velocity field. **(a)** track 86 (ASC). After plate motion correction, the post-seismic signal from the 2013 Khash earthquake (Barnhart et al., 2014) can be more clearly seen in the south-east of the figure. **(b)** track 20 (DSC). **(c)** Location of tracks (a) and (b) and the velocity field of the Eurasian plate, used to correct the tracks. **(i)** Velocity before plate motion correction, but after other corrections have been applied. **(ii)** Velocity after plate motion correction. **(iii)** Applied plate motion correction. **(iv)**. Across track profile of the velocity before plate motion correction. The number below each profile is the gradient of the linear least squares fit to the profile. Note that profiles are plotted as a function of ground range, which increases with distance from the satellite. **(v)** Across track profile of the velocity after plate motion correction. **(vi)** Across track profile of the applied plate motion correction.
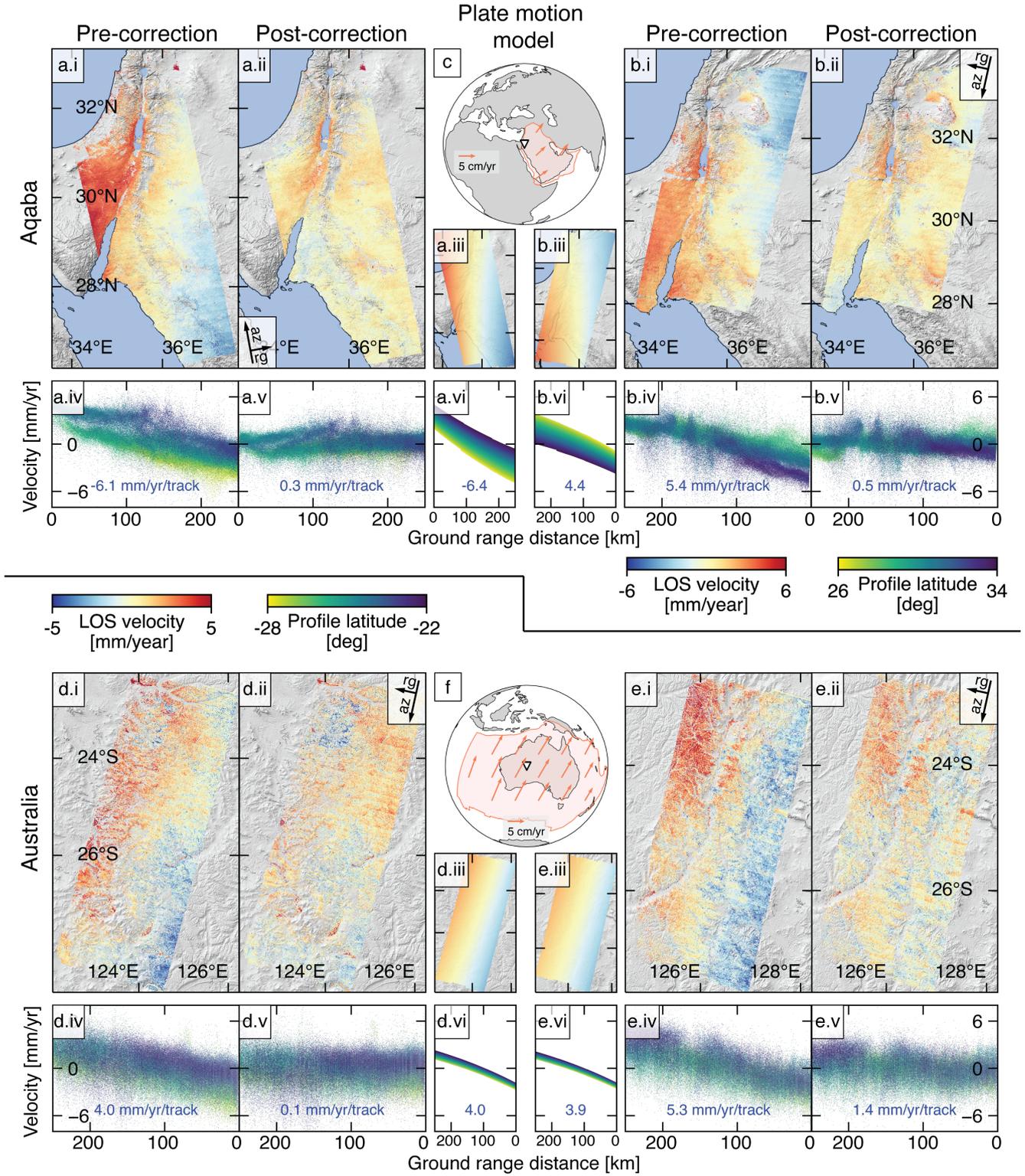
**Figure 4.** Same as Figure 3, but showing the tracks for the Gulf of Aqaba and Australia. **(a)** Gulf of Aqaba, track 87 (ASC). **(b)** Gulf of Aqaba, trac 21 (DSC). **(c)** Location of tracks (a) and (b) and the velocity field of the Arabian plate, used to correct the tracks. **(d)** Australia, track 119 (DSC) **(e)** Australia, track 46 (DSC). **(f)** Location of tracks (d) and (e) and the velocity field of the Australian plate, used to correct the tracks. **(i)-(vi)** are as described in Figure 3.

ten target. See Text S2 for more details on the contributors to long-wavelength residuals.

Deficiencies in the plate motion model, or motion of the InSAR track reference point relative to the assumed plate, could also create long-wavelength residuals. Motion relative to the plate will be of particular importance in areas of diffuse plate boundary deformation, where it is not possible to choose a reference point that is stable with respect to the rigid plate. This could be the case for tracks covering the Makran subduction zone and the Gulf of Aqaba, both of which span plate boundary zones. In these situations, plate motion models may not fully account for the impacts of bulk motion, and using local GNSS measurements to put InSAR measurements into a local terrestrial reference frame could be necessary (Bähr, 2013).

These results emphasise the importance of accounting for the reference frame before interpreting long-wavelength InSAR-derived velocity fields. When using InSAR for studies of tectonic deformation, the most natural reference frame is one that is fixed to a stable region within the scene, so that we can interpret velocity gradients in terms of tectonic strain rather than strain-free translation and rotation. There are several situations in which failing to account for the reference frame could bias the results:

1. Combining multiple tracks to estimate 3D deformation (Fialko et al., 2001; Wright et al., 2004). In Text S4 and Figure S7 we show how plate motion can bias estimates of the 3D velocity field when we use an overlapping ascending and descending track to calculate horizontal and vertical velocities.

2. Modeling InSAR signals. If the long-wavelength signals in an InSAR velocity field are being modeled, and the model is assumed to not be rotating or translating, then a velocity ramp from plate motion may be modeled as strain accumulation and bias the results (e.g. changing the locking depth in a subduction zone model).

3. Comparisons between GNSS and InSAR. Both data sets must be in the same reference frame (Parizzi et al., 2020). If the GNSS are in a local reference frame, the InSAR and GNSS velocities will diverge at long wavelengths due to the signal of plate motion in the InSAR.

Studies which removed ramps from InSAR-derived velocities to account for orbital errors may have inadvertently removed the impact of plate motion in their observations as well, reducing the biases we outlined above.

In this work, our primary focus is on the impact of horizontal plate motions, and we have not considered the contribution of long-wavelength vertical velocities. Horizontal plate motions in ITRF are generally at the scale of centimeters per year (Altamimi et al., 2017), with long-wavelength vertical motions, for example due to post-glacial rebound, significantly smaller at millimeters per year (e.g. Riddell et al. (2020); Lau et al. (2020)). If an InSAR track is taken within a region that is experiencing constant vertical motion, this motion will also create a velocity ramp in the satellite LOS velocity field, but with ASC and DSC tracks having opposite gradients (Figure 1(c)). However, the amplitude of vertical velocities will result in smaller velocity gradients across the satellite track than those caused by horizontal motion (Text S3, Figure S6).

## 6 Conclusion

We have illustrated how InSAR velocity measurements are sensitive to tectonic plate motion in the satellite reference frame. This motion will induce ramps in the InSAR velocity fields, predominantly in the satellite range direction, of up to several millimeters per year. In all of our multi-year time series, plate motion was the dominant long-wavelength signal after ionospheric and tropospheric corrections were applied. We have presented a simple adjustment method, which uses plate motion models to remove the plate motion signal from the InSAR velocity field. This adjustment substantially reduces long-wavelength ramps in multiple InSAR tracks from three different regions of the Earth. Routinely accounting for plate motion in InSAR could reduce biases when constraining long-wavelength tectonic strain induced by local geophysical phenomena. This adjustment is likely to be particularly useful where GNSS is not available to constrain the long-wavelength deformation. The signal of plate motion in InSAR data could also be used to improve plate motion models, which may be helpful where GNSS observations are sparse but high-quality InSAR data are available.

## 7 Open Research

The Sentinel-1 data were provided by the European Space Agency and downloaded from the Alaska Satellite Facility. InSAR data were processed using the InSAR Scien-

tific Computing Environment (ISCE) (Rosen et al., 2012), available at: `https://github`

`.com/isce-framework/isce2`. Time series analysis was performed using the MintPy soft-

ware (Yunjun et al., 2019), available at: `https://github.com/insarlab/MintPy`. Our

plate motion correction method is implemented in MintPy as `bulk_plate_motion.py`

(for review purposes this is available at: `https://github.com/yuankailiu/MintPy/blob/`

`GRL/mintpy/bulk_plate_motion.py`). Other data processing was performed using Python.

Plots were produced using Matplotlib and Cartopy in Jupyter Notebooks, available at

`https://zenodo.org/record/6606282`.

### Acknowledgments

### References

Agram, P. S., Jolivet, R., Riel, B., Lin, Y. N., Simons, M., Hetland, E., ... Lasserre, C. (2013). New Radar Interferometric Time Series Analysis Toolbox Released. *Eos, Transactions American Geophysical Union*, *94*(7), 69–70. Retrieved from `http://doi.wiley.com/10.1002/2013EO070001` doi: 10.1002/2013EO070001

Altamimi, Z., Métivier, L., & Collilieux, X. (2012). ITRF2008 plate motion model. *Journal of Geophysical Research: Solid Earth*, *117*(7), 1–14. doi: 10.1029/2011JB008930

Altamimi, Z., Métivier, L., Rebischung, P., Rouby, H., & Collilieux, X. (2017). ITRF2014 plate motion model. *Geophysical Journal International*, *209*(3), 1906–1912. doi: 10.1093/gji/ggx136

Altamimi, Z., Rebischung, P., Métivier, L., & Collilieux, X. (2016). ITRF2014: A new release of the International Terrestrial Reference Frame modeling nonlinear station motions. *Journal of Geophysical Research: Solid Earth*, *121*(8), 6109–6131. Retrieved from `http://doi.wiley.com/10.1002/2016JB013098` doi: 10.1002/2016JB013098

Amelung, F., Galloway, D. L., Bell, J. W., Zebker, H. A., & Laczniak, R. J. (1999). Sensing the ups and downs of Las Vegas: InSAR reveals structural control of

land subsidence and aquifer-system deformation. *Geology*, *27*(6), 483. Retrieved from https://pubs.geoscienceworld.org/geology/article/27/6/483-486/207094 doi: 10.1130/0091-7613(1999)027⟨0483:STUADO⟩2.3.CO;2

Ansari, H., De Zan, F., & Parizzi, A. (2021). Study of Systematic Bias in Measuring Surface Deformation with SAR Interferometry. *IEEE Transactions on Geoscience and Remote Sensing*, *59*(2), 1285–1301. doi: 10.1109/TGRS.2020.3003421

Bähr, H. (2013). *Orbital effects in spaceborne synthetic aperture radar interferometry* (Doctoral dissertation). doi: 10.5445/KSP/1000037166

Bähr, H., Samiei-Esfahany, S., & Hanssen, R. F. (2012). On The Effect Of Reference Frame Motion On InSAR Deformation Estimates. *Proceedings of Fringe 2011*.

Barnhart, W. D., Hayes, G. P., Samsonov, S. V., Fielding, E. J., & Seidman, L. E. (2014). Breaking the oceanic lithosphere of a subducting slab: The 2013 Khash, Iran earthquake. *Geophysical Research Letters*, *41*(1), 32–36. doi: 10.1002/2013GL058096

Bekaert, D., Walters, R., Wright, T., Hooper, A., & Parker, D. (2015). Statistical comparison of InSAR tropospheric correction techniques. *Remote Sensing of Environment*, *170*, 40–47. Retrieved from https://linkinghub.elsevier.com/retrieve/pii/S0034425715301231 doi: 10.1016/j.rse.2015.08.035

Berardino, P., Fornaro, G., Lanari, R., & Sansosti, E. (2002). A new algorithm for surface deformation monitoring based on small baseline differential SAR interferograms. *IEEE Transactions on Geoscience and Remote Sensing*, *40*(11), 2375–2383. Retrieved from http://ieeexplore.ieee.org/document/1166596/ doi: 10.1109/TGRS.2002.803792

Biggs, J., Wright, T., Lu, Z., & Parsons, B. (2007). Multi-interferogram method for measuring interseismic deformation: Denali Fault, Alaska. *Geophysical Journal International*, *170*(3), 1165–1179. doi: 10.1111/j.1365-246X.2007.03415.x

Chaussard, E., Johnson, C. W., Fattahi, H., & Bürgmann, R. (2016). Potential and limits of InSAR to characterize interseismic deformation independently of GPS data: Application to the southern San Andreas Fault system. *Geochemistry, Geophysics, Geosystems*, *17*(3), 1214–1229. Retrieved from https://onlinelibrary.wiley.com/doi/10.1002/2015GC006246 doi: 10.1002/2015GC006246

Chen, C. W., & Zebker, H. A. (2002). Phase unwrapping for large SAR interfero-grams: Statistical segmentation and generalized network models. *IEEE Transactions on Geoscience and Remote Sensing*, *40*(8), 1709–1719. doi: 10.1109/ TGRS.2002.802453

Cong, X., Balss, U., Eineder, M., & Fritz, T. (2012). Imaging Geodesy—Centimeter-Level Ranging Accuracy With TerraSAR-X: An Update. *IEEE Geoscience and Remote Sensing Letters*, *9*(5), 948–952. Retrieved from `http://ieeexplore .ieee.org/document/6170871/` doi: 10.1109/LGRS.2012.2187042

De Zan, F., Parizzi, A., Prats-Iraola, P., & López-Dekker, P. (2014). A SAR interfer-ometric model for soil moisture. *IEEE Transactions on Geoscience and Remote Sensing*, *52*(1), 418–425. doi: 10.1109/TGRS.2013.2241069

Dicaprio, C. J., Simons, M., Kenner, S. J., & Williams, C. A. (2008). Post-seismic reloading and temporal clustering on a single fault. *Geophysical Journal International*, *172*(2), 581–592. doi: 10.1111/j.1365-246X.2007.03622.x

Doin, M. P., Lasserre, C., Peltzer, G., Cavalié, O., & Doubre, C. (2009). Corrections of stratified tropospheric delays in SAR interferometry: Validation with global atmospheric models. *Journal of Applied Geophysics*, *69*(1), 35–50. Retrieved from `http://dx.doi.org/10.1016/j.jappgeo.2009.03.010` doi: 10.1016/j.jappgeo.2009.03.010

Emardson, T. R., Simons, M., & Webb, F. H. (2003). Neutral atmospheric delay in interferometric synthetic aperture radar applications: Statistical description and mitigation. *Journal of Geophysical Research: Solid Earth*, *108*(B5), 1–8. Retrieved from `http://doi.wiley.com/10.1029/2002JB001781` doi: 10.1029/2002JB001781

Fattahi, H., Agram, P., & Simons, M. (2017). A Network-Based Enhanced Spectral Diversity Approach for TOPS Time-Series Analysis. *IEEE Transactions on Geoscience and Remote Sensing*, *55*(2), 777–786. Retrieved from `http://ieeexplore.ieee.org/document/7637021/` doi: 10.1109/TGRS.2016.2614925

Fattahi, H., & Amelung, F. (2013). DEM Error Correction in InSAR Time Series. *Geoscience and Remote Sensing, IEEE Transactions on*, *51*(7), 4249–4259. Retrieved from `http://ieeexplore.ieee.org/document/6423275/` doi: 10.1109/TGRS.2012.2227761

Fattahi, H., & Amelung, F. (2014). InSAR uncertainty due to orbital errors. *Geophysical Journal International*, *199*(1), 549–560. doi: 10.1093/gji/ggu276

Fattahi, H., & Amelung, F. (2015). InSAR bias and uncertainty due to the systematic and stochastic tropospheric delay. *Journal of Geophysical Research: Solid Earth*, *120*(12), 8758–8773. Retrieved from `https://onlinelibrary.wiley.com/doi/abs/10.1002/2015JB012419` doi: 10.1002/2015JB012419

Fattahi, H., Simons, M., & Agram, P. (2017). InSAR Time-Series Estimation of the Ionospheric Phase Delay: An Extension of the Split Range-Spectrum Technique. *IEEE Transactions on Geoscience and Remote Sensing*, *55*(10), 5984–5996. doi: 10.1109/TGRS.2017.2718566

Fialko, Y. (2006). Interseismic strain accumulation and the earthquake potential on the southern San Andreas fault system. *Nature*, *441*(7096), 968–971. doi: 10.1038/nature04797

Fialko, Y., Simons, M., & Agnew, D. (2001). The complete (3-D) surface displacement field in the epicentral area of the 1999 Mw 7.1 Hector Mine earthquake, California, from space geodetic observations. *Geophysical Research Letters*, *28*(16), 3063–3066. doi: 10.1029/2001GL013174

Fournier, T., Pritchard, M. E., & Finnegan, N. (2011). Accounting for Atmospheric Delays in InSAR Data in a Search for Long-Wavelength Deformation in South America. *IEEE Transactions on Geoscience and Remote Sensing*, *49*(10), 3856–3867. Retrieved from `http://ieeexplore.ieee.org/document/5771553/` doi: 10.1109/TGRS.2011.2139217

Gomba, G., Parizzi, A., De Zan, F., Eineder, M., & Bamler, R. (2016). Toward operational compensation of ionospheric effects in SAR interferograms: The split-spectrum method. *IEEE Transactions on Geoscience and Remote Sensing*, *54*(3), 1446–1461. doi: 10.1109/TGRS.2015.2481079

Hanssen, R. F. (2001). *Radar Interferometry: Data Interpretation and Error Analysis* (Vol. 2). Dordrecht: Springer Netherlands. Retrieved from `http://link.springer.com/10.1007/0-306-47633-9` doi: 10.1007/0-306-47633-9

Hersbach, H., Bell, B., Berrisford, P., Hirahara, S., Horányi, A., Muñoz-Sabater, J., ... Thépaut, J. (2020). The ERA5 global reanalysis. *Quarterly Journal of the Royal Meteorological Society*, *146*(730), 1999–2049. Retrieved from `https://onlinelibrary.wiley.com/doi/10.1002/qj.3803` doi:

10.1002/qj.3803

Hooper, A., Bekaert, D., Spaans, K., & Arikan, M. (2012). Recent advances in SAR interferometry time series analysis for measuring crustal deformation. *Tectonophysics*, *514-517*, 1–13. doi: 10.1016/j.tecto.2011.10.013

Johnston, P. J., Filmer, M. S., & Fuhrmann, T. (2021). Evaluation of methods for connecting InSAR to a terrestrial reference frame in the Latrobe Valley, Australia. *Journal of Geodesy*, *95*(10). Retrieved from https://doi.org/10.1007/s00190-021-01560-2 doi: 10.1007/s00190-021-01560-2

Jolivet, R., Agram, P. S., Lin, N. Y., Simons, M., Doin, M.-p., Peltzer, G., & Li, Z. (2014). Improving InSAR geodesy using Global Atmospheric Models. *Journal of Geophysical Research: Solid Earth*, *119*(3), 2324–2341. Retrieved from https://onlinelibrary.wiley.com/doi/abs/10.1002/2013JB010588 doi: 10.1002/2013JB010588

Jolivet, R., Grandin, R., Lasserre, C., Doin, M. P., & Peltzer, G. (2011). Systematic InSAR tropospheric phase delay corrections from global meteorological reanalysis data. *Geophysical Research Letters*, *38*(17), 1–6. doi: 10.1029/2011GL048757

Jolivet, R., Simons, M., Agram, P. S., Duputel, Z., & Shen, Z.-K. (2015). Aseismic slip and seismogenic coupling along the central San Andreas Fault. *Geophysical Research Letters*, *42*(2), 297–306. Retrieved from http://doi.wiley.com/10.1002/2014GL062222 doi: 10.1002/2014GL062222

Lau, N., Borsa, A. A., & Becker, T. W. (2020). Present-Day Crustal Vertical Velocity Field for the Contiguous United States. *Journal of Geophysical Research: Solid Earth*, *125*(10). Retrieved from https://onlinelibrary.wiley.com/doi/10.1029/2020JB020066 doi: 10.1029/2020JB020066

Lazecky, M., & Hooper, A. (2022). InSAR-derived horizontal velocities in a global reference frame. *ESSOAr (preprint)*, 1–14. Retrieved from https://www.essoar.org/doi/abs/10.1002/essoar.10511058.1 doi: https://doi.org/10.1002/essoar.10511058.1

Li, Z., Muller, J. P., Cross, P., & Fielding, E. J. (2005). Interferometric synthetic aperture radar (InSAR) atmospheric correction: GPS, Moderate Resolution Imaging Spectroradiometer (MODIS), and InSAR integration. *Journal of Geophysical Research: Solid Earth*, *110*(3), 1–10. doi: 10.1029/2004JB003446

Li, Z., Wright, T., Hooper, A., Crippa, P., Gonzalez, P., Walters, R., ... Parsons, B. (2016). Towards InSAR everywhere, all the time, with Sentinel-1. *International Archives of the Photogrammetry, Remote Sensing and Spatial Information Sciences - ISPRS Archives*, *41*(July), 763–766. doi: 10.5194/isprsarchives-XLI-B4-763-2016

Liang, C., Agram, P., Simons, M., & Fielding, E. J. (2019). Ionospheric Correction of InSAR Time Series Analysis of C-band Sentinel-1 TOPS Data. *IEEE Transactions on Geoscience and Remote Sensing*, *57*(9), 6755–6773. doi: 10.1109/tgrs.2019.2908494

Mahapatra, P., der Marel, H. v., van Leijen, F., Samiei-Esfahany, S., Klees, R., & Hanssen, R. (2018). InSAR datum connection using GNSS-augmented radar transponders. *Journal of Geodesy*, *92*(1), 21–32. doi: 10.1007/s00190-017-1041-y

Marinkovic, P., & Larsen, Y. (2015). On Resolving the Local Oscillator Drift Induced Phase Ramps in ASAR and ERS1/2 Interferometric Data—The Final Solution. *Fringe 2015 Workshop (ESA SP - 731)*(1), 20.

Massonnet, D., & Feigl, K. L. (1998). Radar interferometry and its application to changes in the Earth's surface. *Reviews of Geophysics*, *36*(4), 441. Retrieved from `http://doi.wiley.com/10.1029/97RG03139` doi: 10.1029/97RG03139

Massonnet, D., Rossi, M., Carmona, C., Adragna, F., Peltzer, G., Feigl, K., & Rabaute, T. (1993). The displacement field of the Landers earthquake mapped by radar interferometry. *Nature*, *364*(6433), 138–142. Retrieved from `http://www.nature.com/articles/364138a0` doi: 10.1038/364138a0

McKenzie, D. P., & Parker, R. L. (1967). The North Pacific: an Example of Tectonics on a Sphere. *Nature*, *216*(5122), 1276–1280. Retrieved from `https://www.nature.com/articles/2161276a0` doi: 10.1038/2161276a0

Merryman Boncori, J. P. (2019). Measuring Coseismic Deformation With Spaceborne Synthetic Aperture Radar: A Review. *Frontiers in Earth Science*, *7*(February), 1–20. doi: 10.3389/feart.2019.00016

Milbert, D. (2018). *solid: Solid Earth Tide.* Retrieved from `https://geodesyworld.github.io/SOFTS/solid.htm`

Morishita, Y., Lazecky, M., Wright, T., Weiss, J., Elliott, J., & Hooper, A. (2020). LiCSBAS: An Open-Source InSAR Time Series Analysis Package Integrated

504      with the LiCSAR Automated Sentinel-1 InSAR Processor.    *Remote Sensing*,
505      *12*(3), 424.     Retrieved from `https://www.mdpi.com/2072-4292/12/3/424`
506      doi: 10.3390/rs12030424

507 Neely, W. R., Borsa, A. A., & Silverii, F.   (2020).   GInSAR: A cGPS Correction for
508      Enhanced InSAR Time Series.   *IEEE Transactions on Geoscience and Remote*
509      *Sensing*, *58*(1), 136–146.    Retrieved from `https://ieeexplore.ieee.org/`
510      `document/8839742/`   doi: 10.1109/TGRS.2019.2934118

511 Parizzi, A., Brcic, R., & De Zan, F. (2021). InSAR Performance for Large-Scale De-
512      formation Measurement.   *IEEE Transactions on Geoscience and Remote Sens-*
513      *ing*, *59*(10), 8510–8520. doi: 10.1109/TGRS.2020.3039006

514 Parizzi, A., Gonzalez, F. R., & Brcic, R.   (2020).   A covariance-based approach to
515      merging InSAR and GNSS displacement rate measurements.   *Remote Sensing*,
516      *12*(2). doi: 10.3390/rs12020300

517 Peter, H.   (2021).   *Copernicus POD Product Handbook: Copernicus Sentinel-1, -2*
518      *and -3 Precise Orbit Determination Service (CPOD)* (Tech. Rep.).    GMV.
519      Retrieved from `https://sentinel.esa.int/documents/247904/4599719/`
520      `Copernicus-POD-Product-Handbook.pdf`

521 Petit, G., & Luzum, B.   (2010).   *IERS Conventions (IERS Technical Note No. 36)*.
522      Frankfurt, Germany. Retrieved from `http://www.iers.org/TN36/`

523 Riddell, A. R., King, M. A., & Watson, C. S. (2020). Present-Day Vertical Land Mo-
524      tion of Australia From GPS Observations and Geophysical Models.   *Journal of*
525      *Geophysical Research: Solid Earth*, *125*(2). doi: 10.1029/2019JB018034

526 Rosen, P. A., Gurrola, E., Sacco, G. F., & Zebker, H.   (2012).   The InSAR scientific
527      computing environment. In *Proceedings of the european conference on synthetic*
528      *aperture radar, eusar* (Vol. 2012-April, pp. 730–733).

529 Simons, M., & Rosen, P. (2015). Interferometric Synthetic Aperture Radar Geodesy.
530      In *Treatise on geophysics* (Vol. 3, pp. 339–385).    Elsevier.    Retrieved from
531      `https://linkinghub.elsevier.com/retrieve/pii/B9780444538024000610`
532      doi: 10.1016/B978-0-444-53802-4.00061-0

533 Tarayre, H., & Massonnet, D.    (1996).    Atmospheric Propagation heterogeneities
534      revealed by ERS-1 interferometry.   *Geophysical Research Letters*, *23*(9), 989–
535      992.    Retrieved from `http://doi.wiley.com/10.1029/96GL00622`    doi: 10
536      .1029/96GL00622

Weiss, J. R., Walters, R. J., Morishita, Y., Wright, T. J., Lazecky, M., Wang, H., ...
Parsons, B. (2020). High-Resolution Surface Velocities and Strain for Anatolia
From Sentinel-1 InSAR and GNSS Data. *Geophysical Research Letters*, *47*(17).
doi: 10.1029/2020GL087376

Wright, T. J., Parsons, B. E., & Lu, Z. (2004). Toward mapping surface deforma-
tion in three dimensions using InSAR. *Geophysical Research Letters*, *31*(1), 1–
5. doi: 10.1029/2003GL018827

Xu, X., & Sandwell, D. T. (2020). Toward Absolute Phase Change Recovery
with InSAR: Correcting for Earth Tides and Phase Unwrapping Ambiguities.
*IEEE Transactions on Geoscience and Remote Sensing*, *58*(1), 726–733. doi:
10.1109/TGRS.2019.2940207

Xu, X., Sandwell, D. T., Klein, E., & Bock, Y. (2021). Integrated Sentinel-1 InSAR
and GNSS Time-Series Along the San Andreas Fault System. *Journal of Geo-
physical Research: Solid Earth*, *126*(11), 1–14. doi: 10.1029/2021JB022579

Xu, Z.-W., Wu, J., & Wu, Z.-S. (2004). A survey of ionospheric effects on space-
based radar. *Waves in Random Media*, *14*(2), S189-S273. Retrieved from
http://www.tandfonline.com/doi/abs/10.1088/0959-7174/14/2/008 doi:
10.1088/0959-7174/14/2/008

Yu, C., Penna, N. T., & Li, Z. (2020). Ocean Tide Loading Effects on InSAR Ob-
servations Over Wide Regions. *Geophysical Research Letters*, *47*(15). doi: 10
.1029/2020GL088184

Yunjun, Z., Fattahi, H., & Amelung, F. (2019). Small baseline InSAR time se-
ries analysis: Unwrapping error correction and noise reduction. *Computers and
Geosciences*, *133*(May), 104331. Retrieved from https://doi.org/10.1016/j
.cageo.2019.104331 doi: 10.1016/j.cageo.2019.104331

Yunjun, Z., Fattahi, H., Pi, X., Rosen, P., Simons, M., Agram, P., & Aoki, Y.
(2022). Range Geolocation Accuracy of C/L-band SAR and its Implications
for Operational Stack Coregistration. *IEEE Transactions on Geoscience and
Remote Sensing*, *2892*(c), 1–1. Retrieved from https://ieeexplore.ieee
.org/document/9759304/ doi: 10.1109/TGRS.2022.3168509

Zebker, H. A., & Villasenor, J. (1992). Decorrelation in interferometric radar echoes.
*IEEE Transactions on Geoscience and Remote Sensing*, *30*(5), 950–959. doi:
10.1109/36.175330

570   Zheng, Y., Fattahi, H., Agram, P., Simons, M., & Rosen, P.     (2022).     On

571        Closure Phase and Systematic Bias in Multilooked SAR Interferometry.

572        *IEEE Transactions on Geoscience and Remote Sensing*, *60*, 1–11.     Re-

573        trieved from `https://ieeexplore.ieee.org/document/9758802/`     doi:

574        10.1109/TGRS.2022.3167648